ADVANCING EARTH AND SPACE SCIENCES

JGR Atmospheres

RESEARCH ARTICLE
10.1029/2024JD042611

Impacts of El Niño-Southern Oscillation on Earth's Radiant Energy Budget

Larry Guan[1], Xinyue Wang[2], Xun Jiang[2], Liming Li[1], and King-Fai Li[3]

[1]Department of Physics, University of Houston, Houston, TX, USA, [2]Department of Earth and Atmospheric Sciences, University of Houston, Houston, TX, USA, [3]Department of Environmental Sciences, University of California, Riverside, CA, USA

Key Points:

- An analysis of the latest data reveals El Niño-Southern Oscillation (ENSO) affects radiant energy budget (REB), confirming previous studies
- Principal component analysis reveals ENSO significantly contributes to the variance of the REB (>21%) and its components (>34%)
- Comparisons between observations and simulations suggests current models do not work well in simulating tropical REB and its ENSO signals

Correspondence to:
L. Guan,
ljguan@uh.edu

Citation:
Guan, L., Wang, X., Jiang, X., Li, L., & Li, K.-F. (2025). Impacts of El Niño-Southern Oscillation on Earth's radiant energy budget. *Journal of Geophysical Research: Atmospheres*, *130*, e2024JD042611. https://doi.org/10.1029/2024JD042611

Received 30 SEP 2024
Accepted 19 MAY 2025

Abstract We investigate the impact of the El Niño-Southern Oscillation (ENSO) (i.e., El Niño and La Niña events) on the radiant energy budget (REB) of our home planet—Earth. Using the most recent and extensive datasets available from CERES energy balanced and filled (CERES-EBAF), we confirm and extend upon prior works. Particularly, we compare the mean El Niño/La Niña radiance anomalies in the tropics to the mean normal state over 2001–2022. Modifications to the energy budget's components (absorbed solar power and emitted thermal power) exceed 10% within the western and central Pacific—up to 20% for net power. Principal component analysis results further suggest that ENSO contributes approximately 34.0%, 44.9%, and 21.3% of the total variance in absorbed power, emitted power, and net power, respectively. Finally, a comparative study between observational data and the numerical simulations suggests that current climate models cannot quantitatively capture the signals of ENSO in Earth's REB even though some of them can reproduce dominant features. Our investigations based on the comprehensive observational datasets for Earth can serve as a foundation for exploring the impacts of large-scale atmospheric and climate processes on the REBs of other planets.

Plain Language Summary The Earth's climate is driven by the difference in solar energy absorbed by the planet versus thermal energy radiated away into space. Recent studies suggest the existence of a small imbalance between these two components, which likely affects the Earth's climate system significantly. Transpiring climate events can also conversely alter our planet's energy budget. We investigate the impacts of the climate events related to El Niño-Southern Oscillation (ENSO) on Earth's radiant energy budget (REB) using the most recent and extensive radiometric data available from CERES energy balanced and filled (CERES-EBAF). Significant correlations between the radiant energy components, REB, and ENSO are revealed, and the climatic impacts of ENSO leave clear signals in the spatiotemporal variations of the radiant energy budget. Furthermore, comparing observations to simulations suggests that current climate models are incapable of quantitatively capturing the ENSO signals in the REB. Finally, the impacts of ENSO on Earth's REB revealed in this study can serve as a foundation for investigating similar relationships on other planets since other planets also have large-scale atmospheric processes.

1. Introduction

The absorbed solar power and the emitted thermal power at the top of a planet's atmosphere constitute the components of a planet's radiant energy budget (REB) (e.g., Conrath et al., 1989; Peixoto & Oort, 1992). As a critical element of a planet's climate system, the REB and its temporal variations are closely linked to climate change on the planet and its thermal evolution. The REB at the top of the atmosphere also establishes boundary conditions for radiative transfer and distribution within a planetary atmosphere, contributing to the development of temperature gradients by differential heating and cooling. Temperature gradients within the atmosphere provide potential energy, which is convertible into kinetic energy that drives atmospheric motions through mechanisms described by the Lorenz energy cycle (e.g., Lorenz, 1955). The exchange of radiant energies between the atmosphere and the surface further complicates atmospheric and climate systems (e.g., Peixoto & Oort, 1992; Read et al., 2016). Therefore, the REB plays a crucial role in the atmospheric dynamics and general circulation of a planet.

Due to the crucial role of the energy budget in Earth's atmosphere and climate, concerted efforts to measure this quantity have a long history (e.g., Ellis & Vonder Haar, 1976; Hunt et al., 1986). Measurements of Earth's REB have achieved significant advancements in the satellite era with two outstanding projects: the Earth Radiation

Budget Experiment (ERBE) (Barkstrom, 1984; Barkstrom & Hall, 1982) and the Clouds and the Earth's Radiant Energy System (CERES) (Loeb, Doelling, et al., 2018; Loeb, Su, et al., 2018; Wielicki et al., 1996). As an improved version of ERBE, CERES offers several advances in measuring Earth's REB compared to its predecessor (Wielicki et al., 2005). As such, CERES datasets have been widely used in recent investigations of Earth's REB and climate change (e.g., Dewitte & Clerbaux, 2018; Huang et al., 2021; Liu et al., 2020; Loeb et al., 2021, 2022; Mayer et al., 2016; Storto et al., 2017; Su et al., 2017).

Based on recent measurements and studies of Earth's REB and oceanic heat content, the Earth's energy budget components (EBC) were discovered to be not in balance—the absorbed solar power is marginally larger than the emitted thermal power (e.g., Allan et al., 2014; Hansen et al., 2005, 2011; Loeb et al., 2012; Trenberth et al., 2014, 2016). In the long run, this tiny imbalance—∼0.2–0.4% of the absorbed solar power—will gradually change Earth's climate (e.g., Hansen et al., 2005, 2011; Trenberth et al., 2014, 2016). On shorter timescales, spatiotemporal variations of radiant energies in the atmosphere and at the surface modify meteorological processes and surface properties (e.g., Peixoto & Oort, 1992; Read et al., 2016). Due to the important roles that the REB plays in global warming and climate change, there are many efforts tracking the spatiotemporal variations of Earth's REB (e.g., Allan et al., 2014; Dewitte & Clerbaux, 2018; Liu et al., 2020; Loeb et al., 2012, 2020, 2021; Loeb, Su, et al., 2018; Trenberth & Fasullo, 2012; Zhu et al., 2016). Conversely, atmospheric and climate events can modify the REB at regional and global scales (e.g., Huang et al., 2021; Loeb, Su, et al., 2018; Matus & L'Ecuyer, 2017; Mayer et al., 2016; Pinker et al., 2017; Su et al., 2017; Zhou et al., 2016). Even transient man-made clouds, such as aviation contrails, have a significant persistent presence in the skies, enough to influence the REB over annual timescales (e.g., Chen & Gettelman, 2016; Dessens et al., 2014; Sausen et al., 2005; Wilcox et al., 2012).

Among the most influential of terrestrial climate phenomena on the global energy budget is the El Niño-Southern Oscillation (ENSO). ENSO-related events recur with periods ranging from 2 to 7 years, characterized by alternately warming (El Niño) and cooling (La Niña) of sea surface temperatures (SST) in the central and eastern tropical Pacific Ocean. El Niño/La Niña events hold significant importance across a wide range of scientific disciplines due to their substantial environmental and socioeconomic impacts. Numerous studies have already investigated the causes and impacts of ENSO (e.g., see the reviews by Cai et al., 2020; Wang et al., 2016), including the perspective of radiative feedbacks (e.g., Dessler, 2013; Huang et al., 2021; Kolly & Huang, 2018; Zhu et al., 2016).

Recognizing ENSO's importance, we re-examine the relationship between ENSO and the REB using the most recent and extensive top-of-atmosphere radiometric datasets provided by CERES, spanning the years 2001–2022. Particularly, we compare the mean El Niño/La Niña radiance anomalies of the tropics to the mean normal state through the lens of spatial analysis and separately apply principal component analysis (PCA) to the data. Finally, characteristics in this analysis are used to provide observational constraints for climate model development. To examine the performance of current climate models, we conduct comparative investigations between the observational dataset (CERES) and simulations by the representative models included in the latest version of the Coupled Model Intercomparison Project (CMIP6) through the lens of PCA (Eyring et al., 2016).

2. Data, Models, and Methodology

In this study, two datasets are utilized. The first dataset is the climate data record of Earth's REB, known as the CERES energy balanced and filled (CERES-EBAF) (Loeb, Doelling, et al., 2018). This record comprises multiple series of radiance measurements initially collected by CERES instruments onboard multiple satellites, which are then processed into instantaneous top-of-atmosphere (TOA) radiant fluxes (Loeb, Doelling, et al., 2018). We employ their measurements of TOA incident solar flux, reflected shortwave flux, outgoing longwave flux, and net flux. The spatial resolution is 1° latitude × 1° longitude over the entire globe, with a monthly temporal resolution spanning from March 2000 to April 2023. Here, we utilize the years with a complete set of months (i.e., 2001–2022) to facilitate the REB comparison between years with El Niño/La Niña events and years without them. For our purpose, absorbed power is calculated by elementwise subtraction of the incident solar flux and reflected shortwave flux measurements, emitted power is simply the outgoing longwave flux, and net power is absorption minus emission.

The other major dataset employed is the monthly Niño 3.4 SST index provided by the Climate Prediction Center at the National Oceanic and Atmospheric Administration (NOAA-CPC). This dataset consists of SST anomaly measurements (i.e., SST measurements with cycles, trends, and the mean removed) within the Niño-3.4 region

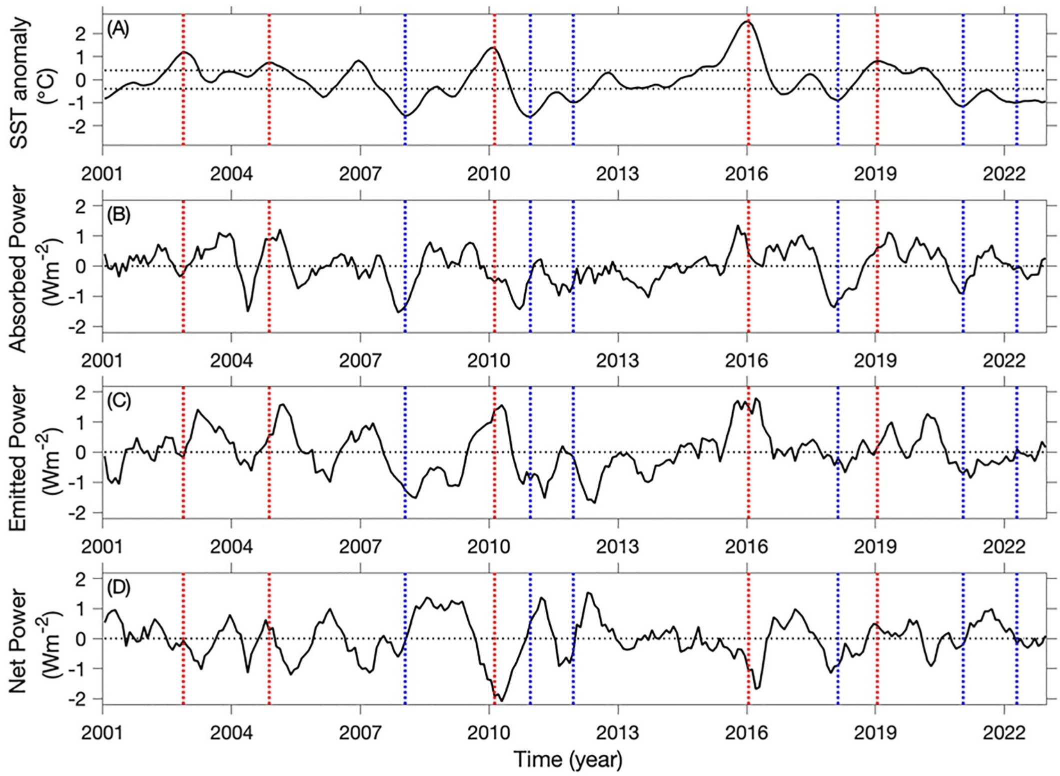

Figure 1. Time series of the Niño 3.4 SST Index and the spatial-average EBCs over the tropical region (20°N–20°S) during the period of 2001–2022. Vertical dashed lines represent the maximal SST anomalies for the El Niño (red lines) and La Niña events (blue lines). (a) Detrended and smoothed monthly El Niño 3.4 SST Index. The two horizontal dashed lines (+0.4°C and −0.4°C) represent the criteria for identifying El Niño and La Niña events, respectively. (b) Detrended and smoothed monthly data for the anomalies of absorbed solar power. Panels (c, d) are similar to panel (b) except for emitted thermal power and net power, respectively.

(latitudes 5°S–5°N, longitudes 190°–240°E) and serves as one way to characterize ENSO activity (Trenberth & Stepaniak, 2001). For this work, the monthly Niño 3.4 SST index is used to represent ENSO activity. Following the recommendation by the National Center for Atmospheric Research (NCAR) (Trenberth & National Center for Atmospheric Research Staff, 2024), El Niño/La Niña events are defined where the 5-month running mean of the Niño 3.4 SST exceeds ±0.4°C for six consecutive months or more. To explore the relationship between the Niño 3.4 SST index and REB, each dataset from CERES-EBAF is first stripped of seasonal cycles, means, and linear trends, as was applied to the Niño 3.4 SST index. For consistency, we also compute 5-month running means for the CERES-EBAF fluxes.

Based on the Niño 3.4 SST data (panel A of Figure 1) and the definition of El Niño/La Niña events, 5 El Niño events and 6 La Niña events were identified from 2001 to 2022 (Table 1). In this study, we aim to examine the differences in Earth's REB between years with and without El Niño/La Niña events, so we assume that each El Niño/La Niña event lasts 1 year to facilitate interannual comparisons. For El Niño/La Niña events where the 5-

Table 1
List of Periods When El Niño or La Niña Events Occurred

Event	Period
El Niño	July 2002–June 2003; August 2004–July 2005; July 2009–June 2010; July 2015–June 2016; October 2018–September 2019
La Niña	July 2007–June 2008; July 2010–June 2011; July 2011–June 2012; November 2017–October 2018; August 2020–July 2021; October 2021–September 2022

Note. Periods not listed in this table during 2001–2022 are defined as normal periods or years.

10.1029/2024JD042611

month running mean of the Niño 3.4 SST index exceeds ±0.4°C for 12 months or fewer, we designate the first month in the sequence and the following 11 months as an El Niño/La Niña year. For El Niño/La Niña events where the rolling mean threshold is exceeded for more than 12 consecutive months, we designate the 12 months with the most extreme SST anomalies as an El Niño/La Niña year. The periods of the 5 El Niño events and 6 La Niña events are listed in Table 1.

Our investigation is restricted to the tropical latitudes spanning 20°N to 20°S. Three approaches are applied. First, we examine the correlations between the time series of the Niño 3.4 SST index and the spatial-average fluxes over the tropics. Next, we compare the spatial patterns of the flux anomalies between the years with El Niño/La Niña events and normal years. Finally, we investigate the dominant modes of each EBC and the net power using PCA.

To temporally explore the relationship between the Niño 3.4 SST index and the REB, each of the flux datasets from the CERES-EBAF is first spatially averaged over the 20°N–20°S latitude range to obtain a time series for absorbed power, emitted power, and net power. Then, each time series is stripped of seasonal cycles, means, and linear trends. Finally, we calculate the 5-month running mean of each time series to maintain consistency with the data processing procedure applied to the Niño 3.4 SST index.

To spatially compare the EBCs between years with El Niño/La Niña events and normal years, we first divide the raw monthly CERES-EBAF data into three groups based on the temporal delineations presented in Table 1: (a) data corresponding to the periods of 5 El Niño events, (b) data corresponding to the 6 La Niña events, and (c) the remaining data (referred to as normal years). Then, data in the three groups are temporally averaged to obtain time-mean tropical maps. Finally, spatial differences in the radiant energies between El Niño/La Niña years and normal years are determined by subtracting the normal-year map from the El Niño/La Niña maps.

We lastly conduct PCA on the CERES-EBAF fluxes. PCA involves decomposing a multivariable dataset into spatial empirical orthogonal functions (EOFs), which are mutually orthogonal eigenfunctions of the covariance matrix associated with the dataset. Each EOF has an associated eigenvalue, and a corresponding time-dependent amplitude called the principal component (PC) time series. The leading EOF, associated with the largest eigenvalue, captures the plurality of the dataset's variance (e.g., Camp et al., 2003). The main takeaways of this procedure are: PCA acts such as a generalized Fourier transform useful for datasets with high dimensionality (i.e., CERES-EBAF) and the leading EOF in the context of our study will showcase the most persistent spatial flux distribution (e.g., Jiang et al., 2004, 2008a, 2008b; Trammell et al., 2016). To prepare the CERES-EBAF datasets for PCA, the raw fluxes (i.e., time series of fluxes at each grid point of the tropical maps) are stripped of seasonal cycles, means, and linear trends. Then, a lowpass filter is applied to the time series at each grid point, which removes high frequency signals with periods <15 months (Jiang et al., 2004) and suppresses short period phenomena such as the phase locking of ENSO to the boreal winter (Stuecker et al., 2013) and the Madden-Julian oscillation (Jiang et al., 2020). The PCA technique is then applied to the detrended and filtered fluxes.

Finally, we comparatively examine the results of our analysis based on the CERES-EBAF data against simulations from climate models to assess their performance. In this study, we use outputs from CMIP6 (Eyring et al., 2016) to examine Earth's REB. The Coupled Model Intercomparison Project (CMIP) is an initiative led by the World Climate Research Programme (WCRP) to improve our understanding of climate change by comparing and analyzing different climate models. The absorbed solar power, emitted power, and net power from 15 representative models included in CMIP6 (ACCESS, AWI, BCC, CAMS, CanESM5, CESM2, CMCC, FIO, GISS, HadGEM3, IITM, MIROC, MPI, MRI, and NESM) are analyzed in this study.

Outputs from the 15 CMIP6 models stop in December 2014, and the observational dataset from CERES-EBAF spans 21 years (2001–2021). To ensure temporal parity between CERES-EBAF and CMIP6, both datasets are bounded to the period of January 2001 to December 2014. PCA is subsequently applied to the truncated datasets. Namely, PCA is applied to the absorbed solar power, emitted thermal power, and net power from 2001 to 2014, where the processed results between observations and simulations are finally compared visually.

3. Results

3.1. Correlation Between ENSO and Energy Budget Components

We first discuss correlations between the time series of the El Niño 3.4 SST index (panel a, Figure 1) and that of the absorbed, emitted, and net powers (panels b–d, Figure 1). Following the criteria provided by NCAR, 5 El Niño

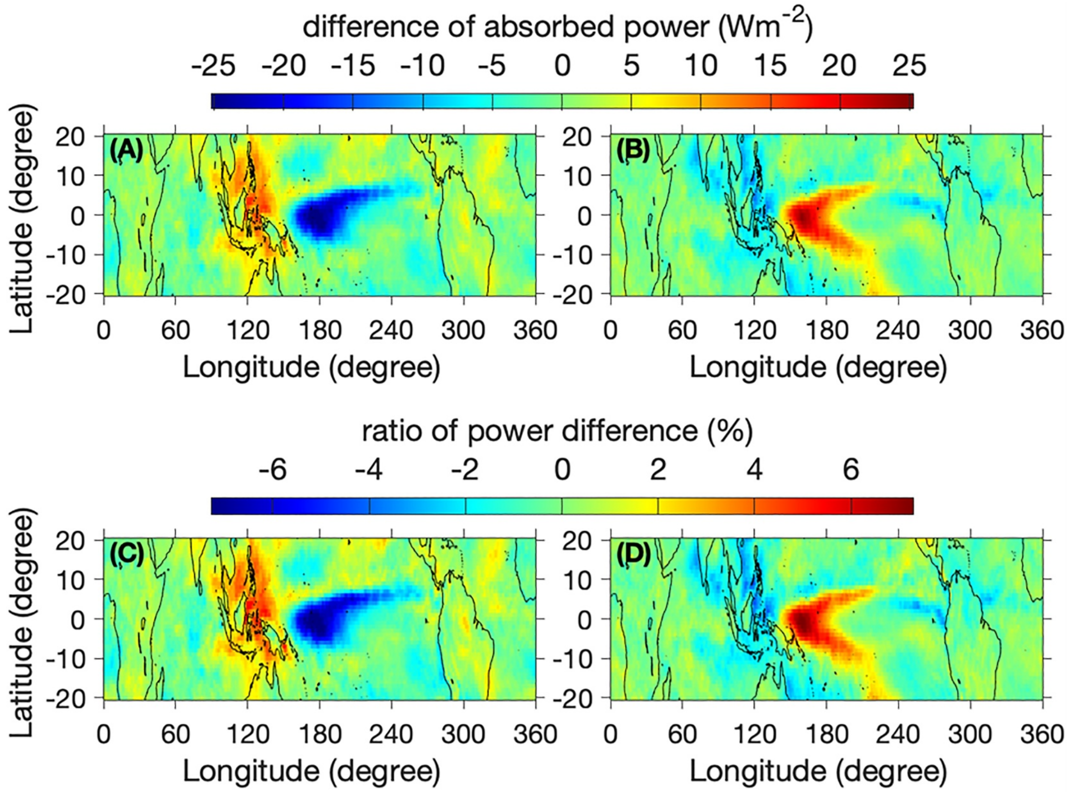

Figure 2. Difference in the absorbed solar power over the tropical region (20°N–20°S) between the years with El Niño/La Niña events and normal years. (a) Difference in the absorbed solar power between the years with El Niño events and normal years. (b) Difference in the absorbed solar power between the years with La Niña events and normal years. (c) Ratio between the power difference during El Niño events (panel a) and the time-mean absorbed solar power. (d) Ratio between the power difference during La Niña events (panel b) and the time-mean absorbed solar power. The time-mean absorbed solar power is based on data from normal years only.

events (vertical red dashed lines) and 6 La Niña events (vertical blue dashed lines) are identified using the El Niño 3.4 SST index from 2001 to 2022 (Table 1). The computed correlation coefficients between the SST index and each irradiance timeseries are 0.45, 0.74, and −0.39 for the absorbed solar power, the emitted thermal power, and the net power, respectively.

Confidence levels of the computed correlation coefficients are examined using a Monte Carlo method (Press et al., 1992), which was also used in our previous study (Jiang et al., 2004). Isospectral surrogate time series are generated for each of the three irradiance timeseries presented in Figure 1 (panels b–d), and between each of the isospectral time series and the Niño 3.4 SST index, a set of correlation coefficients associated with each series is generated. Then, the distribution of each generated set of correlation coefficients is transformed into a normal distribution. Confidence levels of the correlation coefficients between the Niño 3.4 SST index and the non-surrogate irradiances can now be determined by examining their positions on the distribution—reading 99%, 99%, and 98% for absorbed, emitted, and net powers respectively. Therefore, as expected, the time series of radiant energies over the tropical region all bear significant correlation with El Niño/La Niña events.

3.2. Variations of the Energy Budget Components Caused by El Niño/La Niña Events

To explore the physics behind the significant correlations between the EBCs and El Niño/La Niña events (Figure 1), we investigate the spatial differences in EBCs between the years with El Niño/La Niña events and normal years, as described in "Data, Models, and Methodology." Figure 2 illustrates the difference in the absorbed solar power between the years with El Niño/La Niña events and normal years, which is associated with the Walker circulation adjustment to ENSO (e.g., Larkin & Harrison, 2005; Li, Chen, & Lu, 2023; Zhou et al., 2019). Panel A of Figure 2 shows the anomaly of absorbed power during the El Niño years relative to the normal years. During El Niño events, the Walker circulation is significantly weakened, causing the upwelling branch to shift from the western Pacific Ocean to the central Pacific Ocean, where clouds predominantly form. Clouds generally have a much higher albedo than oceans, which increases reflected solar flux and consequently decreases absorbed power over the central Pacific during El Niño events. This explains the minimum center observed in the map of the absorbed power over the central Pacific Ocean (panel a of Figure 2). The eastward shift of the upwelling branch of the Walker circulation and the associated clouds also results in relatively clear skies around the western Pacific Ocean during El Niño. As such, the absorbed power increases over the western Pacific during El Niño events.

Panel b of Figure 2 displays the change in the absorbed power during La Niña events. La Niña events exhibit characteristics opposite to those of El Niño events. With an enhanced Walker circulation during La Niña events, more clouds develop from the strengthened upwelling in the western Pacific Ocean, while clear skies result from the strengthened downwelling in the central Pacific Ocean. This creates an observable inverted configuration in the change of absorbed power during La Niña events (panel b) compared to the morphology of El Niño events (panel a). Panels a and b of Figure 2 suggest that extremal deviations in the absorbed power over the Pacific Ocean can reach ~20 Wm^{-2} during ENSO years, or ~6% of the time-mean absorbed solar power during normal years, as depicted in panels c and d of Figure 2.

Based on the spatial distribution of the absorbed solar power presented in Figure 2, we examine the net change in spatial-average absorbed power over the entire tropical region (20°N–20°S). Panel a of Figure 2 shows that the area around the western Pacific Ocean with increased solar power is larger than the area of the central Pacific Ocean with decreased solar power. Therefore, we anticipate a positive net change in absorbed power during El Niño events across the tropical region. Computation of the spatial average over the entire tropical region confirms this point: the spatial-average absorbed power increases by approximately 0.18 Wm^{-2} during El Niño events, representing about 0.06% of the time-mean absorbed power.

For the absorbed solar power during La Niña events (panel b of Figure 2), the area around the western Pacific Ocean reporting a decrease is likewise larger than the area within the central Pacific Ocean reporting an increase. Consequently, a negative net change in absorbed power is expected and observed during La Niña events: the spatial-average absorbed power decreases by ~0.44 Wm^{-2}, representing about 0.14% of the time-mean absorbed power. The positive and negative changes in spatial-average absorbed power during El Niño and La Niña events, respectively, reinforce the positive correlation between the El Niño 3.4 SST index and the time series of the absorbed power shown in Figure 1.

Now, let us examine the emitted thermal power. Figure 3 illustrates the difference in the emitted power between the years with El Niño/La Niña events and normal years. First, notice that the spatial patterns are roughly the same between the emitted (Figure 3) and absorbed powers (Figure 2). This is reasonable because clouds associated with the Walker circulation play an important role in both EBCs. When the ocean and land are covered by clouds, thermal emission from clouds are the dominant outgoing thermal power and they generally have colder temperatures (i.e., emit less power compared to land and ocean). Clouds can also create a greenhouse effect by trapping the comparatively stronger surface thermal emission (e.g., Philander, 1990; Salby, 1996; Wang et al., 2016). Therefore, clouds over the central Pacific Ocean, shifted east from the western Pacific Ocean during El Niño events, contribute to decreasing the emitted power over the central Pacific Ocean (panel a of Figure 3) and generate a warming mechanism by increasing net power. Simultaneously occurring higher thermal emission from the western Pacific surface under relatively clear skies increases the emitted power over this region during El Niño events. On the other hand, more clouds in the western Pacific and clearer skies in the central Pacific during La Niña events help explain the negative and positive centers over the two regions, respectively, as shown in panel b of Figure 3. Averaging over the whole tropical region, we find that spatial-average emitted power increases by ~0.87 Wm^{-2} during El Niño events (0.34% of the time-mean emitted power) and decreases ~0.55 Wm^{-2} during La Niña events (0.21% of the time-mean emitted power).

While Figures 2 and 3 have roughly identical morphologies, the magnitude and spatial extent of the difference in radiant powers caused by El Niño/La Niña events are smaller for the absorbed power (Figure 2) than for the emitted power (Figure 3). Unlike emitted thermal power, which is determined by longwave radiation from clouds and the surface, absorbed solar power is controlled not only by the reflection/scattering of clouds and the surface but also by incident solar power. Moreover, reflection/scattering is a complex process that depends not only on the optical characteristics of clouds and the surface but also on their physical properties (e.g., particle size). On the

10.1029/2024JD042611

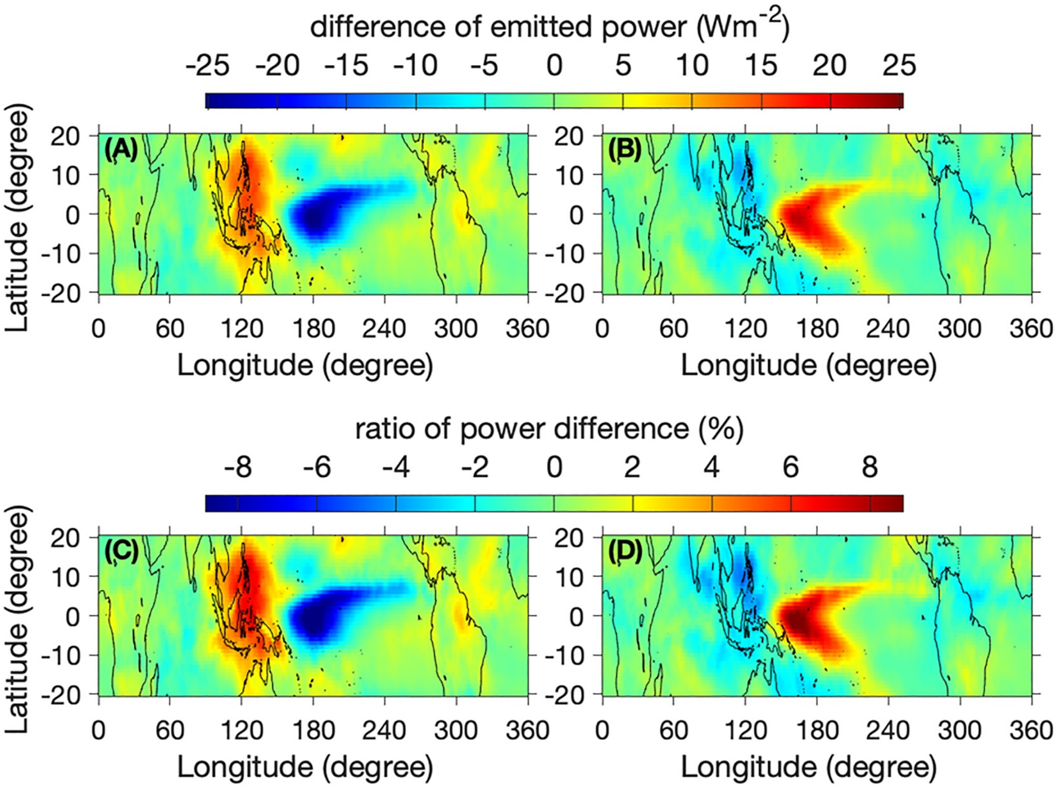

Figure 3. Same as Figure 2 except now for the difference in the emitted thermal power between the years with El Niño/La Niña events and normal years.

other hand, outgoing thermal fluxes are mainly determined by the cloud and surface temperatures. The complexity of reflection/scattering can weaken the relationship between El Niño/La Niña events and the absorbed solar power, thereby explaining the relatively smaller magnitude and spatial coverage of the modification in the absorbed power compared to those in the emitted power.

Figure 4 presents the difference in the net power between the years with El Niño/La Niña events and normal years. The absorbed power and emitted power act antagonistically on Earth's net power. By convention, absorption positively contributes to net power while emission negatively contributes. Figures 2 and 3 show that changes in radiant powers during El Niño/La Niña events have similar morphology, which implies that changes caused by El Niño/La Niña events in the absorbed power and emitted power mostly negate each other. The antagonism between absorbed and emitted powers contributes to the smaller correlation coefficient between the El Niño 3.4 SST index and the time series of net power determined from Figure 1. For the spatial-average tropical net power, it decreases by ~0.69 Wm^{-2} during El Niño events (1.3% of the time-mean net power) and increases ~0.11 Wm^{-2} during La Niña events (0.20% of the time-mean net power). It should be noted that the variances in spatial-average net energy and constituent EBCs attributable to El Niño/La Niña events are around 1% or less. These variances are comparable in magnitude to the global-average energy imbalance (~0.2–0.4%) (e.g., Hansen et al., 2011; Trenberth et al., 2014).

Quite apparently, the difference centers caused by El Niño/La Niña events over the western and central Pacific Oceans in the absorbed power (Figure 2) and emitted power (Figure 3), essentially vanish in the net power (Figure 4). However, because the magnitudes and spatial extents of the difference centers over the tropical Pacific are smaller for absorbed power than for emitted power, the two EBCs do not fully cancel each other, resulting in residual differences across the Pacific Ocean (panels a and b of Figure 4) that can reach up to 20% of the time-mean net power for some locations (panels c and d of Figure 4)—over twice that for the absorbed and emitted powers shown in Figures 2 and 3 (~6%–8%). This significantly larger difference ratio rises from the relatively small magnitude of net power compared to those of the absorbed and emitted powers. Additionally, panels c and

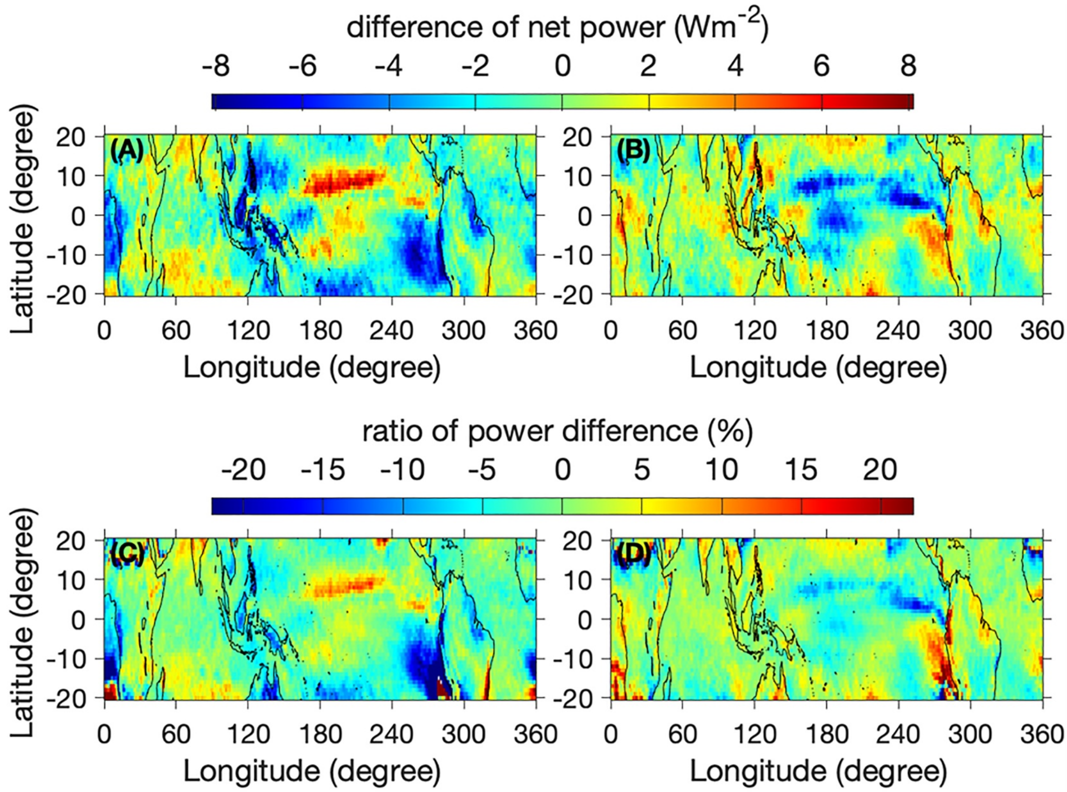

Figure 4. Same as Figure 2 except now for the difference in the net power between the years with El Niño/La Niña events and normal years.

d of Figure 4 show that the strongest and most spatially extensive percentage differences in the net power caused by El Niño/La Niña events are not found at the same locations as previously seen in panels c and d of Figures 2 and 3. Here, they are located off the South American Pacific and the African Atlantic coasts. PCA of the net power discussed in the next section demonstrates that these centers are also related to the ENSO, which exemplifies ENSO's ability to remotely and drastically influence local energy budgets.

As a specific case, we examine the impacts of the strongest El Niño event (2015–2016 event) and La Niña event (2010–2011 event) on Earth's REB. Figure 5 suggests that the ratio of energy differences caused by the strongest El Niño/La Niña events against their respective time-mean EBCs are approximately double compared to those caused by the average of all El Niño/La Niña events (Figures 2–4). Particularly, the difference ratios caused by the strongest El Niño/La Niña events can exceed 10% for both the absorbed power (panels a and b) and emitted power (panels c and d). Regarding the net power, the difference ratio can reach 20% in the Pacific Ocean, the region where ENSO directly acts, though isolated regions further afield can exceed 30% due to its teleconnection to local atmospheric and climate processes.

3.3. PCA of Energy Budget Components (2001–2021)

The time series (Figure 1) and the spatial patterns of the EBCs (Figures 1–4) suggest that El Niño/La Niña events play a critical role in modifying radiant energies over the Pacific Ocean. To further examine the dominant modes modifying the EBCs during El Niño/La Niña events, we conduct PCA. Figure 6 displays the results of PCA applied to the absorbed solar power over the tropical region. Panel A of Figure 6 illustrates the spatial pattern of the first EOF (EOF 1), capturing ∼34.0% of the variance in the absorbed power. The leading mode morphologically resembles the dominant spatial pattern revealed in our power difference analysis for absorbed power between the years with El Niño/La Niña events and other years (Figure 2). In panel B of Figure 6, the corresponding principal component (PC1) is plotted against the Niño 3.4 SST index. These two curves show a strong correlation over the data's time frame, with a correlation coefficient of 0.87 (99% confidence level). Spectral

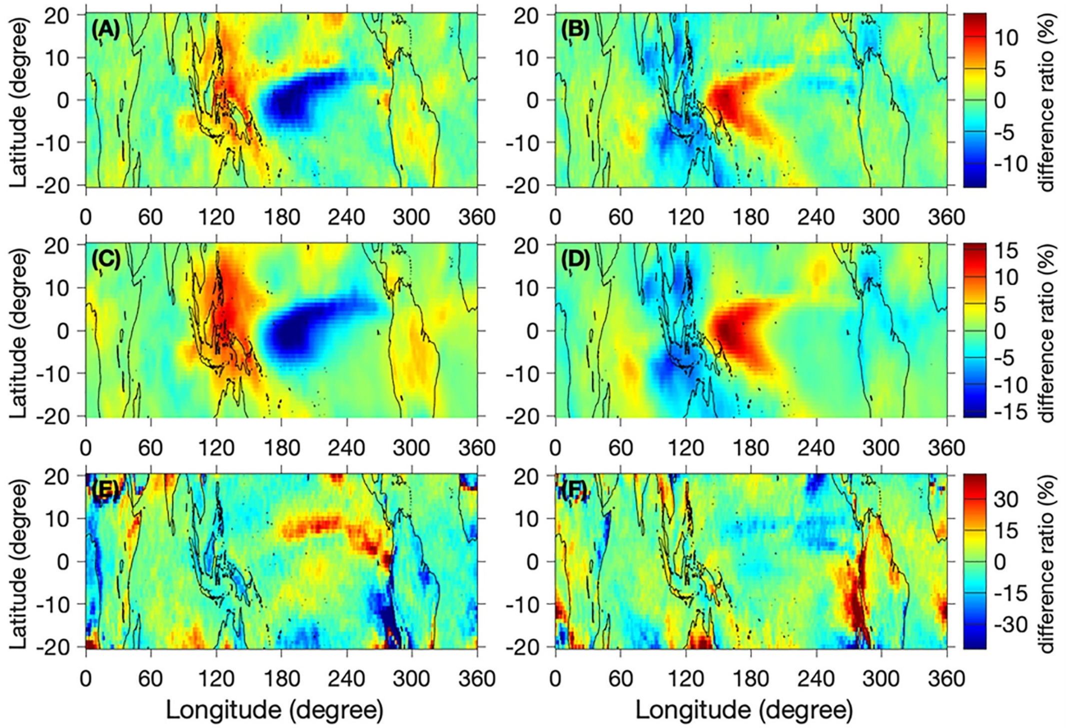

Figure 5. Power difference ratio between the strongest El Niño/La Niña events and the time-mean power. (a) Ratio between the difference in the absorbed solar power for the strongest El Niño event (the 2015–2016 event) and the time-mean absorbed solar power. (b) Ratio between the difference in the absorbed solar power for the strongest La Niña event (the 2010–2011 event) and the time-mean absorbed solar power. Panels (c, d) are the same as panels (a, b) respectively, except for the emitted thermal power. Panels (e, f) are the same as panels (a, b) respectively, except for the net power.

analysis of PC1 presented in panel C suggests that the most prominent periods of the signals are between approximately 2 and 7 years, which are consistent with the periods of El Niño/La Niña events.

Figure 7 presents PCA for the emitted thermal power over the tropical region. First, PCA reveals some similarities between the absorbed solar power (Figure 6) and the emitted power (Figure 7). Panel a shows that the leading mode of emitted power has essentially the same morphology as that of the leading mode in the absorbed power (see panel a of Figure 6). However, the magnitudes and spatial extents of the two centers over the western and central Pacific oceans in the leading mode are larger in the emitted power (Figure 7) than in the absorbed power (Figure 6). This is reasonable because the power difference in the EBCs between the years with El Niño/La Niña events and normal years (Figures 2 and 3) also suggests the same result. The leading mode presented in panel a of Figure 7 captures ∼44.9% of the variance in the emitted power, which is larger than the 34.0% variance captured for the absorbed power. The subsequent panel of Figure 7 (panel b) plots PC1 against the Niño 3.4 SST index, revealing a strong correlation coefficient of ∼0.87 (99% confidence level) between them. The power spectrum of PC1 (panel C of Figure 7) also suggests that the prominent periods of the signals are between approximately 2 and 7 years.

Finally, PCA of the net power is presented in Figure 8. Panel a displays the spatial pattern of the first EOF, where ∼21.3% of the variance in the net power is captured. Compared to the leading EOFs of the absorbed and emitted powers (Figures 6 and 7), the first EOF in the net power captures less variance. Much like in our power difference analysis, variances in the absorbed and emitted powers partially negate each other's contribution. Additionally, the leading mode's structure over the western and central Pacific oceans is similar to the spatial pattern revealed in our analysis of power differences in the net power between the years with El Niño/La Niña events and normal years (Figure 5). Panel b of Figure 8 portrays a strong correlation between the PC1 of net power and the Niño 3.4 SST index, measuring ∼0.84 (99% confidence level). Such a high correlation coefficient is more statistically significant than the correlation coefficient between the El Niño 3.4 SST index and the spatial-average net power over the tropical region (∼−0.39). The spatial average of the first mode has a negative value, so the spatial-

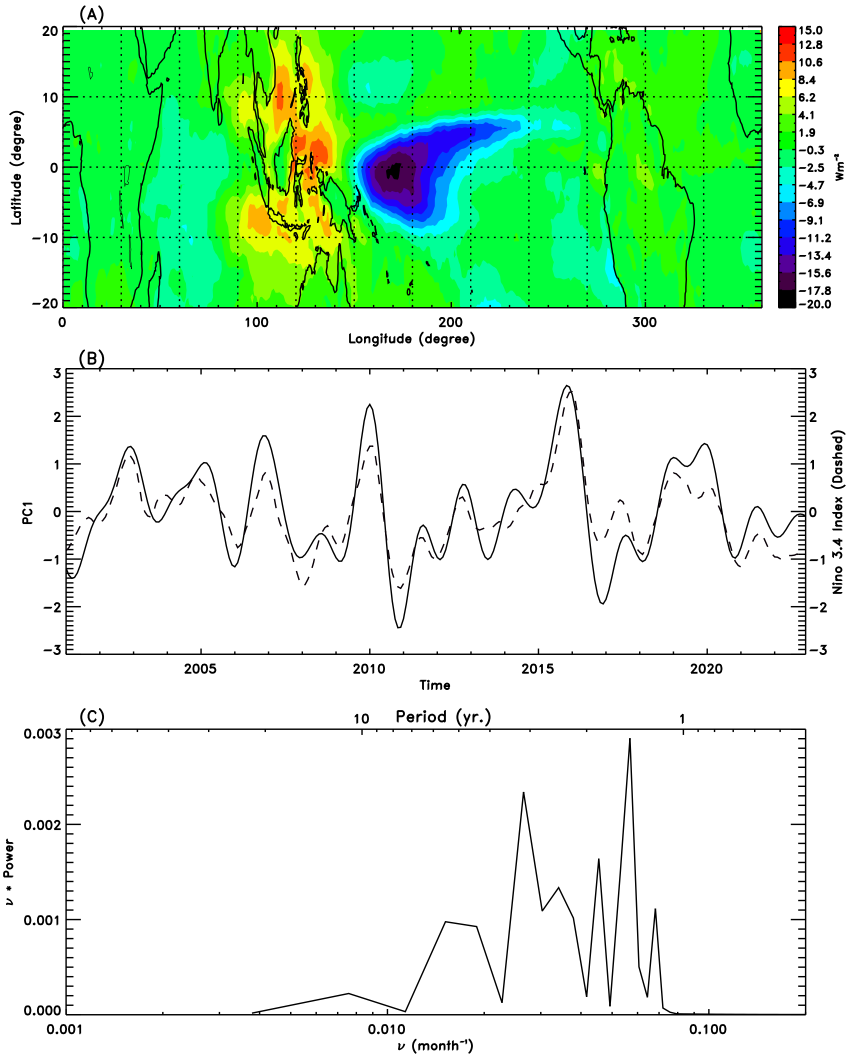

Figure 6. PCA of the absorbed solar power over the tropical region. (a) Spatial map of the leading mode or first EOF (EOF1). (b) Comparison between the PC corresponding to the EOF1 (PC1) (solid line) and the Niño 3.4 SST index (dashed line). (c) Power spectrum of PC1.

average net power over the tropical region is weakly anticorrelated with the Niño 3.4 SST index (Figure 1d). Meanwhile, the spatial-average net power (Figure 1d) includes foreign signals beyond ENSO, which weakens the correlation between the spatial-average net power and the Niño 3.4 SST index. Summarily, ENSO signals in the net power over the tropical region are better revealed by PCA as compared to the analysis of time series (Figure 1) and power difference (Figure 4).

3.4. Comparison of PCA Between Observations and Simulations (2001–2014)

Inspired by prior studies (Dessler, 2013; Kolly & Huang, 2018) that scrutinized the performance of prior generations of the CMIP models by comparing their outputs to observational data, we will also examine the performance of the current generation of climate models through the lens of PCA. Specifically, as discussed in the section of "Data, Models, and Methodology," the 15 representative models comprising CMIP6. We conduct the PCA on the EBCs for both observations and simulations during the period of 2001–2014 and provide a comparative overview of their outputs.

A comparison of the absorbed solar power is displayed in Figure 9. First, EOF1 from observations of the absorbed solar power (CERES-EBAF) shows nearly identical morphology between the periods 2001–2021 (panel a of

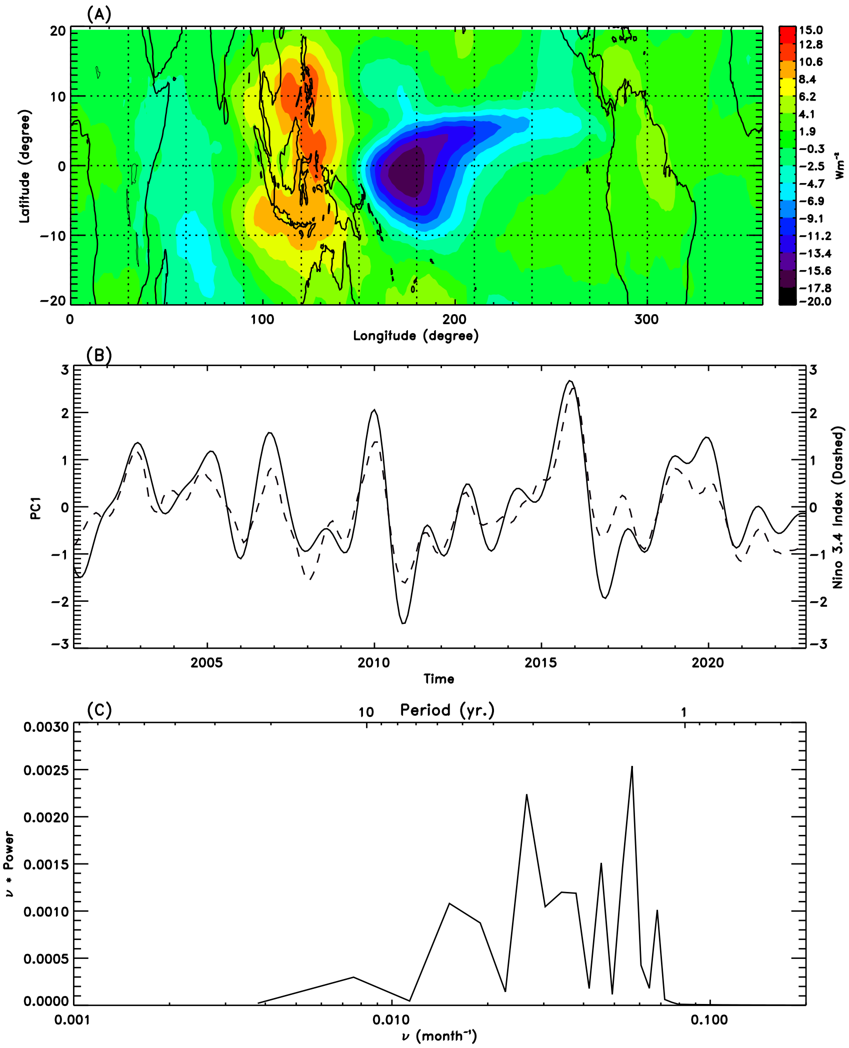

Figure 7. Same as Figure 6 except now for the PCA of the emitted thermal power.

Figure 6) and 2001–2014 (panel a of Figure 9). Both maps showcase the main characteristics of the variance in absorbed solar power caused by El Niño/La Niña events: a positive center in coastal areas near the western Pacific and a more prominent negative center over the central Pacific Ocean. A few CMIP6 simulation outputs successfully captured the pair of dominating positive and negative centers (Figure 9, panels b, g, h, i, j, k, m, o, and p), but the remaining models (Figure 9, panels c, d, e, f, l, and n) produce an incorrect number of centers or render them in incorrect locations. Even in models that successfully generate the two dominant centers, there are notable discrepancies in magnitude and extent between the observations and simulations.

Figure 10 presents the EOF1 maps for the emitted thermal power from observations and simulations. Like with observations of absorbed solar power between the periods 2001–2021 (panel a of Figure 7) and 2001–2014 (panel a of Figure 10), EOF1 for emitted thermal power based on observations exhibits nearly identical morphology over the western and central Pacific Oceans. However, unlike the results of PCA on the absorbed solar power, models better captured the main characteristics of the variance in emitted thermal power caused by El Niño/La Niña events: a positive center in coastal areas near the western Pacific with a more dominant negative center in the central Pacific Oceans. This suggests that the CMIP6 models perform better in simulating emitted thermal power than absorbed solar power, which is reasonable given that absorbed solar power is influenced by more complex physical and dynamic processes in the atmosphere and at the surface compared to emitted thermal power (see Section 3.2). Unfortunately, there remains significant discrepancies in magnitude and spatial extent between the observations and simulations.

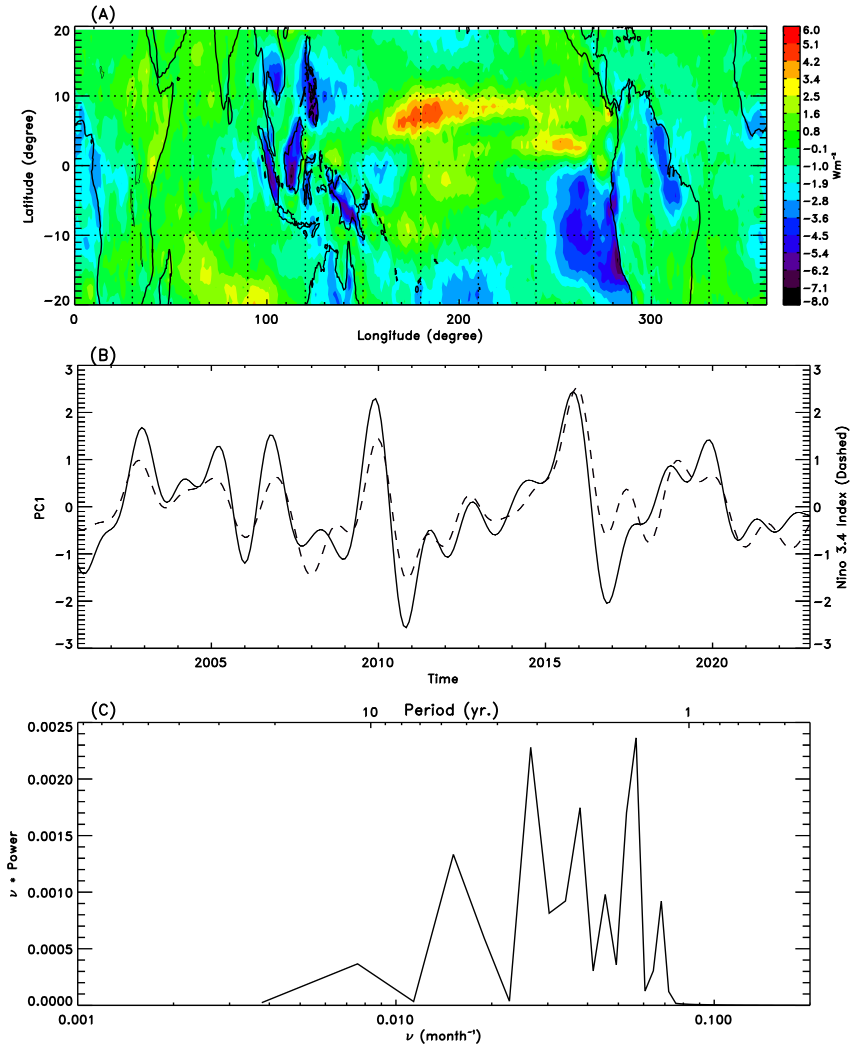

Figure 8. Same as Figure 6 except now for the PCA of the net power.

The comparison of EOF1 maps for the net power between observations and simulations is presented in Figure 11. Extremely large discrepancies between observation and simulation for the net power are exhibited both quantitatively and qualitatively for almost all models. Succinctly, CMIP6 models cannot reproduce observed patterns of the variance in the net power caused by El Niño/La Niña events. Since the net power is the combined result of both the absorbed solar power and emitted thermal power, discrepancies between observations and simulations in the absorbed solar power (Figure 9) and emitted thermal power (Figure 10) compound in the net power and manifest as extreme discrepancies in Figure 11.

The PC1 time series for each leading mode of absorbed solar power (Figure 9), emitted thermal power (Figure 10), and net power (Figure 11) are displayed in the three panels of Figure 12. The panels show that PC1 for CERES-EBAF observations (thick black solid line) correlates well with the Niño 3.4 SST index (blue dashed line) for the absorbed solar power (panel a), emitted power (panel b), and net power (panel c). However, the time series for CMIP6 model simulations (colored solid lines) are largely out of phase with the Niño 3.4 SST index time series in all panels. Figure 12 also shows that the standard deviation of the simulations from the 15 models (gray areas) is relatively large, which is comparable to the magnitude of the observations. This suggests that there are significant differences among the simulations produced by the 15 models. Consequently, the averages of the PC time series for all models for absorbed solar power, emitted thermal power, and net power (thin black solid lines) exhibit much smaller variations than those in the observations (thick black solid lines).

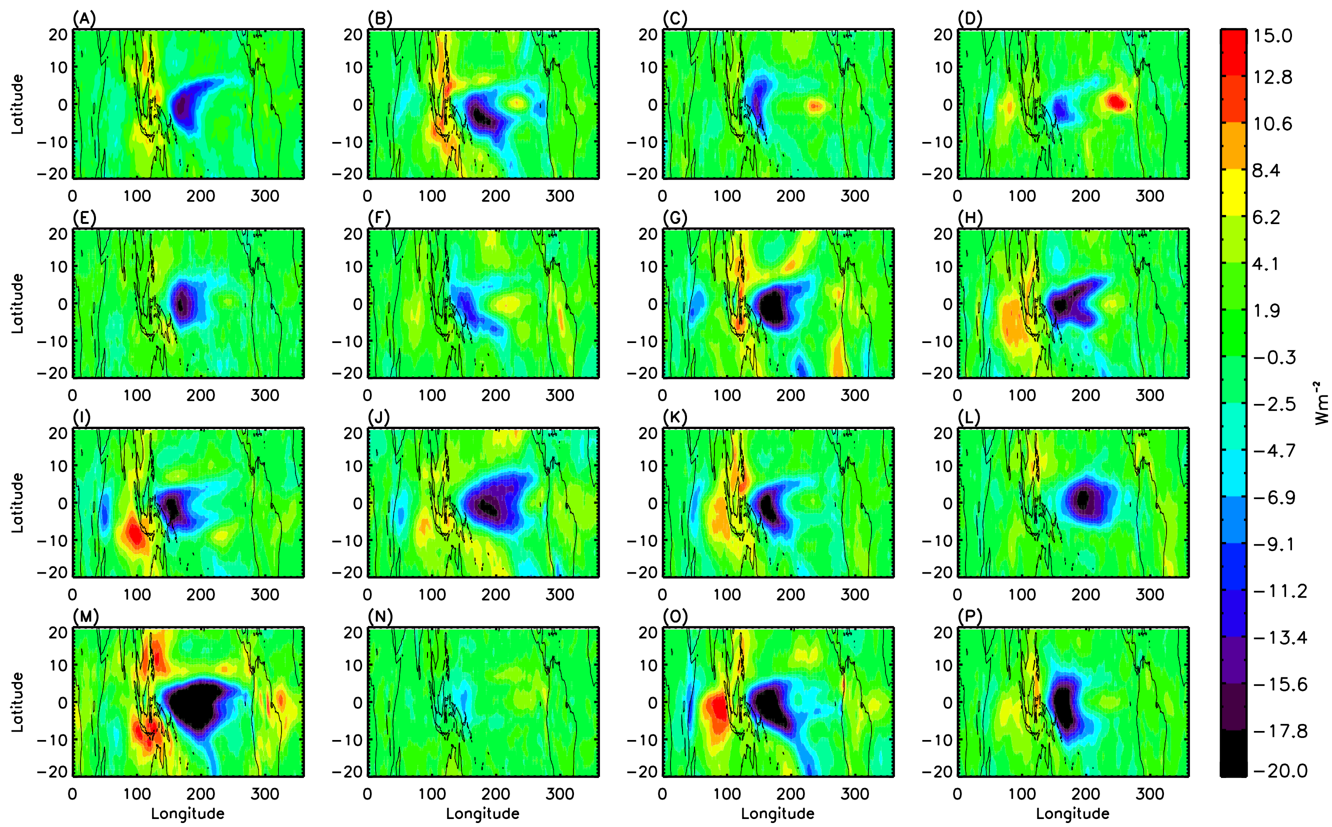

Figure 9. Comparison of EOF1 for absorbed solar power between CERES-EBAF observations and CMIP6 models (2001–2014). Panel (a) corresponds to the observations of CERES-EBAF. The remaining panels are for CMIP6 simulations in the following order: (b) ACCESS, (c) AWI, (d) BCC, (e) CAMS, (f) CanESM5, (g) CESM2, (h) CMCC, (i) FIO, (j) GISS, (k) HadGEM3, (l) IITM, (m) MIROC, (n) MPI, (o) MRI, and (p) NESM.

Computing the correlation coefficients between the observations and the Niño 3.4 SST index timeseries yields values of 0.80, 0.80, and 0.79 for the absorbed solar power, emitted thermal power, and net power, respectively. In contrast, the correlation coefficients between the 15 simulations and the Niño 3.4 SST index are always lower than 0.37, 0.34, and 0.39 for the absorbed solar power, emitted thermal power, and net power, respectively. Furthermore, the correlation coefficients between the averages of the PC time series for all models (thin black solid lines in Figure 12) and the Niño 3.4 SST index are less than 0.1. These results indicate that the CMIP6 models have significant limitations in accurately simulating the phases of El Niño/La Niña events and their impact on Earth's EBCs.

Since the CMIP6 models do not accurately reproduce the observed ENSO signal, we instead turned to verifying the self-consistency of each model. The Niño 3.4 sea surface temperature (SST) was computed directly from the CMIP6 models, where a lowpass filter was then applied to the modeled Niño 3.4 SST to isolate the low-frequency variability. The correlation coefficients between the PC1 of model absorbed solar radiation and the filtered model Niño 3.4 SST range from 0.76 to 0.96. For emitted thermal radiation, the correlation coefficients range from 0.71 to 0.97, and for the net radiative power, from 0.75 to 0.97. Despite the models' limitations in simulating the ENSO signal, strong correlations exist between the modeled SSTs and model radiative fluxes, which suggests a fair state of operability.

To further reinforce inconsistencies between models and observations, we directly compare the tropical REB between observations (Figure 1) and numerical simulations, as shown in Figure 13. This figure illustrates that all simulated time series of the REB from CMIP6 models (colored solid lines) are significantly out of phase with the observed time series (black lines). The standard deviations of the simulations from the 15 models (gray areas in Figure 13) are comparable to the magnitudes of the observations, which also suggests large discrepancies among the simulations by the 15 models. The standard deviation of observed absorbed solar power is 0.57 W/m^2, while the CMIP6 models exhibit a range from 0.32 to 1.13 W/m^2. For emitted thermal power, the observed standard

Journal of Geophysical Research: Atmospheres 10.1029/2024JD042611

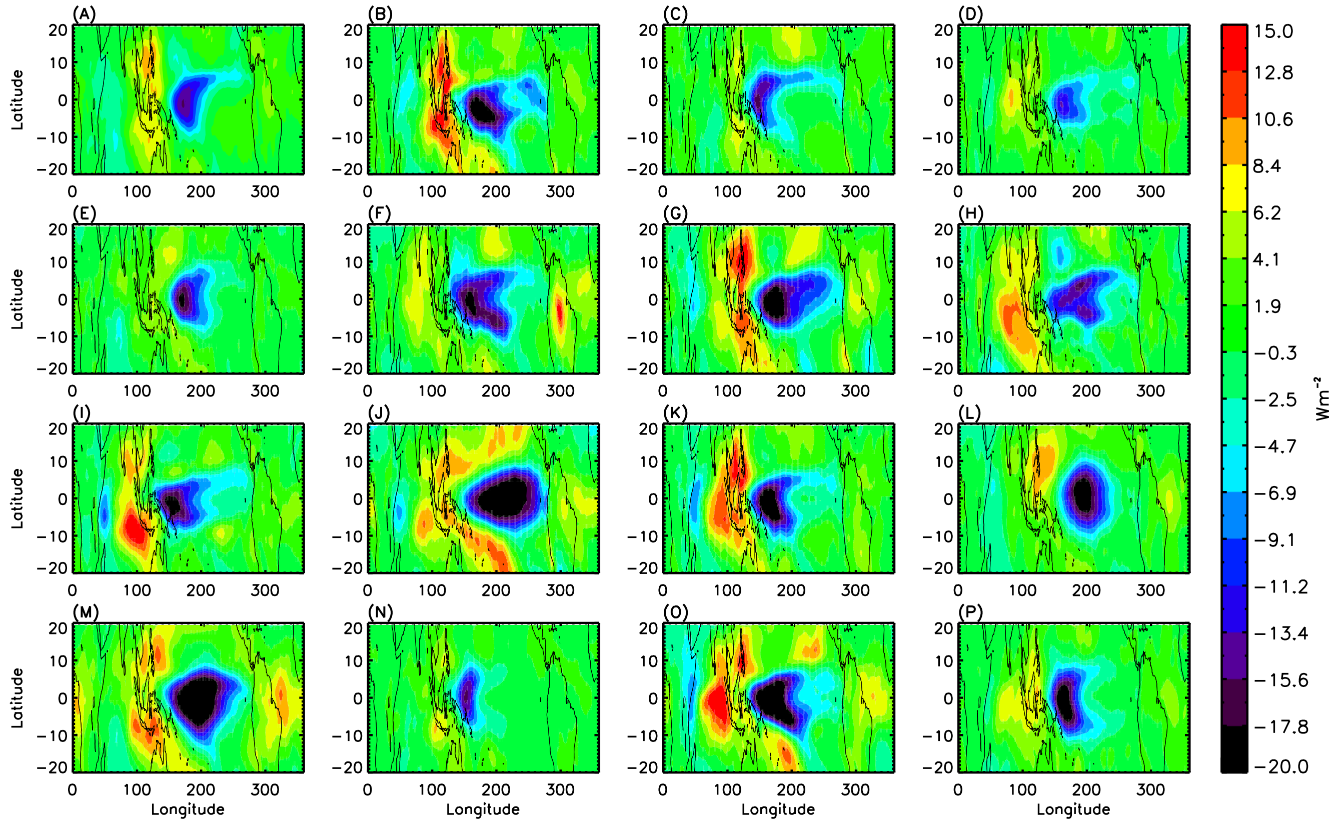

Figure 10. Same as Figure 9 except for emitted thermal power.

deviation is 0.75 W/m^2, compared to a range of 0.44–1.21 W/m^2 in the CMIP6 models. Regarding the net radiative power, the observed standard deviation is 0.74 W/m^2, whereas the CMIP6 values range from 0.57 to 1.30 W/m^2. These discrepancies suggest that the CMIP6 models do not accurately simulate the tropical REB. Consequently, we conclude that the CMIP6 models perform poorly in reproducing the tropical REB and its dominant ENSO signals. Possible reasons for the poor performance of the CMIP6 models are likely related to the models' limitations in simulating SST, the thermal and optical properties of clouds, and the interactions between the atmosphere and oceans. Future work pursuing systematic investigations of the models' performance concerning the REB and the related radiative feedback could be valuable for improving climate models.

4. Conclusion and Discussion

We have used the latest version of the CERES dataset, spanning the last two decades (2001–2022), to examine the impacts of El Niño/La Niña events on Earth's REB within the tropical region. Particularly, we compared the mean El Niño/La Niña state of the tropics to its mean neutral conditions over the aforementioned time frame. The temporal characteristics of the spatial-average EBCs show significant correlations with El Niño/La Niña events. Spatial modifications caused by El Niño/La Niña events on the absorbed and emitted powers mainly occur in the western and central Pacific oceans and are attributed to changes to the Walker circulation, which alter cloud distributions across the surface. As for the net power, contributions from each EBC combine and manifest proportionally large spatial energy modifications away from the Niño-3.4 region (in excess of 20%), which highlights ENSO's ability to remotely influence climate patterns. Most prominently, large percentage differences from local time-mean values are associated with variations in clouds near the western coasts of South America and Africa between El Niño/La Niña events and neutral years (Cai et al., 2020; Didi et al., 2023).

PCA further quantifies the extent of spatial modifications to each EBC. While PCA is not a novel technique in studies of terrestrial EBCs, prior studies have focused their attention on the emitted or absorbed powers individually and typically considered shorter temporal periods such as diurnal and seasonal (e.g., Mlynczak

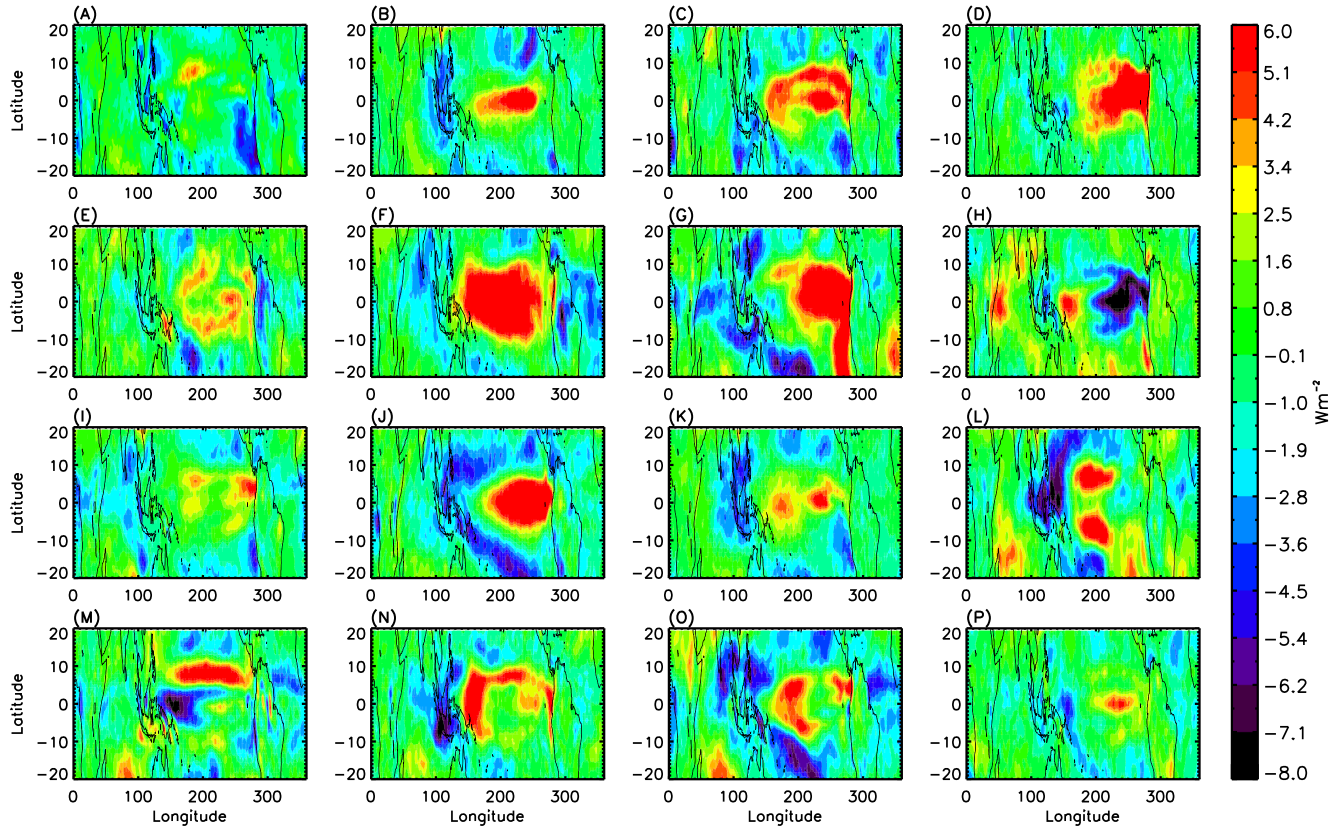

Figure 11. Same as Figure 9 except now for the net power.

et al., 2011; Smith et al., 2012). Here, we focus on longer-period variations. Namely, after filtering out short-period oscillations (<15 months), ENSO is the dominant mode within the absorbed, emitted, and net powers in 2001–2022. The leading modes of absorbed, emitted, and net power were determined to capture 34.0%, 44.9%, and 21.3% of their respective variance and have pronounced peaks in their spectra within a range of 2–7 years. Longer period oscillations of the decadal scale contributed negligibly. The only visible spectral peak in the decadal regime likely corresponds to the 11-year sunspot cycle (Li & Tung, 2023) and is substantially smaller than the peaks within the subdecadal regime.

Our comparative analysis between observational datasets and CMIP6 simulations under the lens of PCA suggest that current models generally simulate the emitted thermal power better than the absorbed solar power because the latter is more susceptible to influence by the more complicated physical and dynamic processes. Although some CMIP6 models can capture the dominant spatial patterns of the absorbed and emitted powers, all CMIP6 models fail to reproduce the numerical range of variance in the EBCs caused by El Niño/La Niña events as seen in observations. Simulations of net power by the CMIP6 models are the least accurate because of imperfections in simulating each EBC compound when simulating the net power. The sensitivity to initial inaccuracy is so extreme that none of the CMIP6 models can capture the basic patterns of variance in net power caused by El Niño/La Niña events.

While El Niño/La Niña events significantly impact the tropical REB, there is also a potential feedback mechanism from the REB on these events. From a broader perspective, this feedback can be interpreted as the influence of the REB on surface temperature, including sea surface temperatures in the Pacific Ocean—an essential factor in the initiation and development of El Niño/La Niña events. Although some studies (e.g., Hansen et al., 2005; Huang et al., 2021; Radley et al., 2014; Shell et al., 2008; Trenberth et al., 2010, 2015) have explored this feedback, it remains highly complex. Comprehensive investigations of such a feedback mechanism would need to address key processes, including the radiative transfer of absorbed solar power from the top of the atmosphere to the

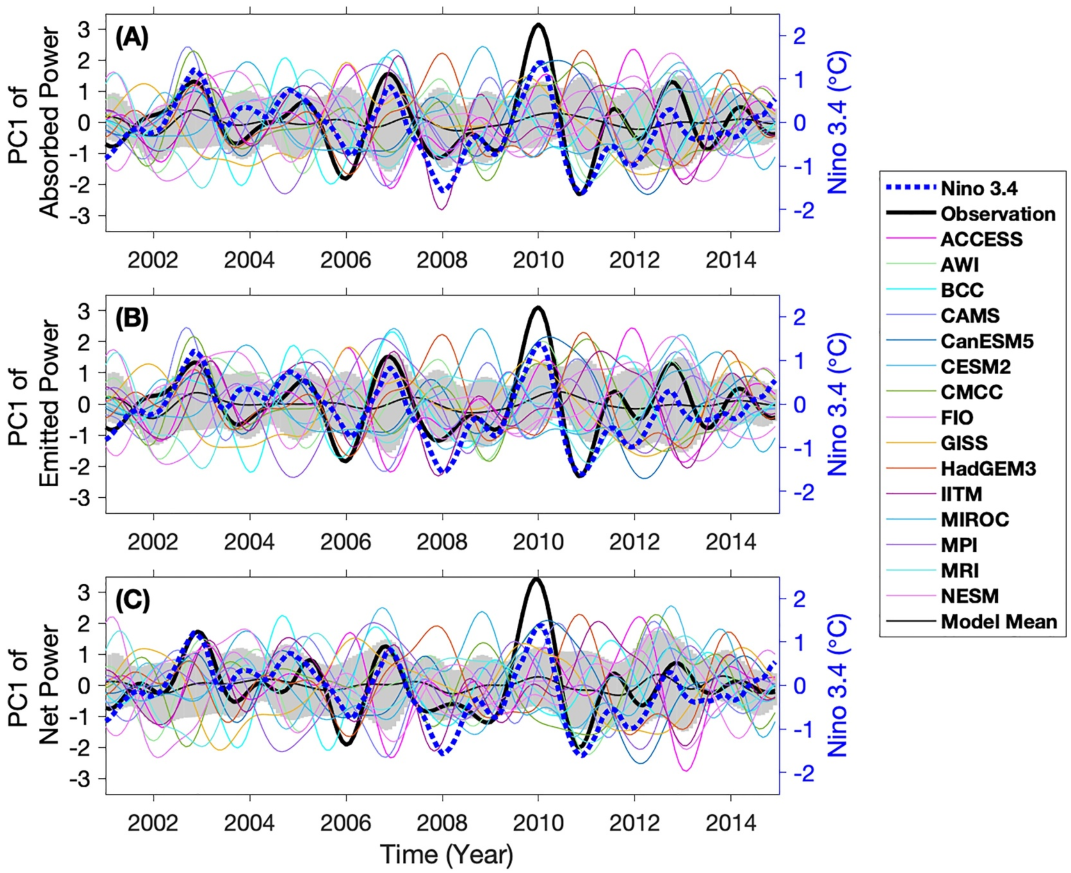

Figure 12. Comparison of PC time series of the leading mode of Earth's tropical EBCs between observations and simulations from the CMIP6 models. (a) Absorbed solar power. (b) Emitted thermal power. (c) Net power. The Niño 3.4 SST index (dashed blue line) is also included in the three panels. The thin black solid line in each panel represents the average of the PC time series for all models (i.e., the model mean). The gray areas illustrate the standard deviation of the PC time series for all models. Specifically, the top boundary of the gray area corresponds to the average value plus the standard deviation of the PC time series for all models, while the bottom boundary represents the average value minus the standard deviation.

atmosphere and surface, energy transformations (e.g., Lorenz energy cycle), atmospheric and oceanic circulation, and atmosphere-surface interactions. These aspects are important topics for future research.

As a final consideration, our investigation can also serve as a ground reference for similar studies on other planets. However, quantitative studies of this nature are relatively limited because current observations of other planets lack the necessary resolution and coverage. Observations and prior studies have revealed the presence of large-scale atmospheric processes that similarly and significantly modify the REBs of other planets such as Mars and Saturn (e.g., Creecy et al., 2021, 2022; Hanel et al., 2003; Li et al., 2012, 2015, 2018; G. Li et al., 2023; L. Li et al., 2023; Wang et al., 2024). Much like El Niño/La Niña events on Earth, these events recur quasi-periodically (e.g., Li & Ingersoll, 2015; Martin & Zurek, 1993; Sánchez-Lavega et al., 2011) with a probable connection to the spatiotemporal variations of their REBs (Creecy et al., 2022; Wang et al., 2024). In the future, when measurements with improved spatiotemporal resolution become available, reanalysis of planetary energy budgets and their interactions with atmospheric and climate processes using the approaches employed in this work would be an insightful and important undertaking.

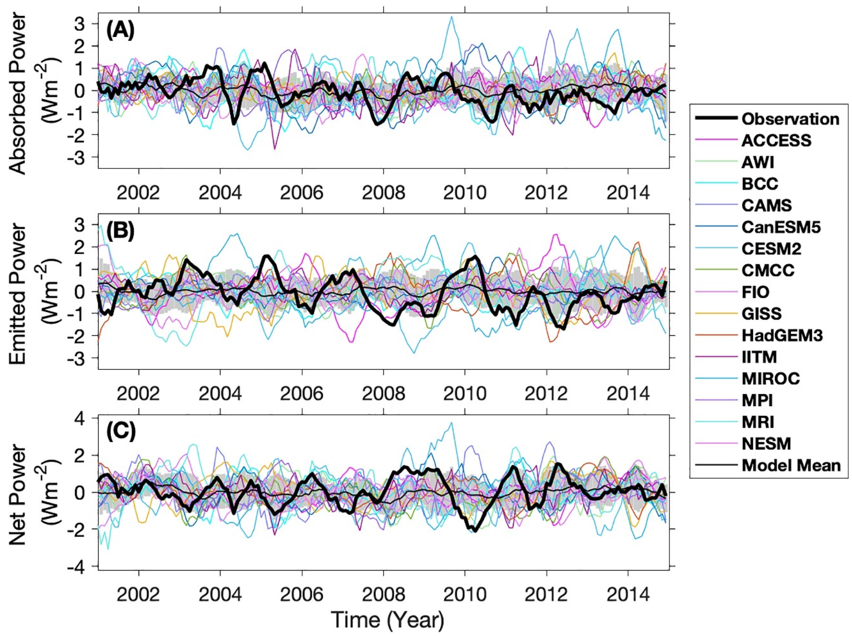

Figure 13. Direct comparison of Earth's tropical EBCs between observations and simulations from the CMIP6 models. (a) Absorbed solar power. (b) Emitted thermal power. (c) Net power. The thin black solid line in each panel represents the average of the energy time series for all models (i.e., the model mean). The gray areas illustrate the standard deviations of the PC time series for all models. Specifically, the top boundary of the gray area corresponds to the average value plus the standard deviation of the energy time series for all models, while the bottom boundary represents the average value minus the standard deviation.

Data Availability Statement

The CERES-EBAF data used in this study are publicly available online from the NASA Langley Research Center and can be downloaded (Doelling, 2022). The following settings were used: "Parameters" was unchanged; "Monthly" for Temporal Resolution, both "Regional" and "Zonal mean" for Spatial Resolution (constrain latitudes to −20 South and 20 North), and Time Range "01-2001" to "12-2022." Technical information pertaining to this dataset is discussed by Loeb, Doelling, et al. (2018). The El Niño 3.4 SST index is also publicly accessible online from the NOAA-CPC website (National Center for Atmospheric Research Staff, 2024). Specifically, the set of data under the heading "Monthly ERSSTv5 (centered base periods) Niño 3.4 (5°North–5°South) (170–120° West)" was selected. Procedures behind its procurement is extensively discussed by Huang et al. (2017). Outputs for the CMIP6 model simulations are also available online (Copernicus Climate Change Service, 2021).

Acknowledgments
We thank the teams working on CERES-EBAF and at NOAA-CPC for recording, processing, archiving, and keeping their respective datasets updated. Additionally, we acknowledge the CMIP6 team for generating and archiving the datasets from the simulations made by the 15 models comprising CMIP6.

References

Allan, R. P., Liu, C., Loeb, N. G., Palmer, M. D., Roberts, M., Smith, D., & Vidale, P. (2014). Changes in global net radiative imbalance 1985–2012. *Geophysical Research Letters*, *41*(15), 5588–5597. https://doi.org/10.1002/2014gl060962

Barkstrom, B. R. (1984). The Earth radiation budget experiment (ERBE). *Bulletin of the American Meteorological Society*, *65*(11), 1170–1185. https://doi.org/10.1175/1520-0477(1984)065<1170:terbe>2.0.co;2

Barkstrom, B. R., & Hall, J. B., Jr. (1982). Earth radiation budget experiment (ERBE): An overview. *Journal of Energy*, *6*(2), 141–146. https://doi.org/10.2514/3.62584

Cai, W., McPhaden, M. J., Grimm, A. M., Rodrigues, R. R., Taschetto, A. S., Garreaud, R. D., et al. (2020). Climate impacts of the El Niño–Southern Oscillation on South America. *Nature Reviews Earth and Environment*, *1*(4), 215–231. https://doi.org/10.1038/s43017-020-0040-3

Camp, C. D., Roulston, M. S., & Yung, Y. L. (2003). Temporal and spatial patterns of the interannual variability of total ozone in the tropics. *Journal of Geophysical Research*, *108*(D20), 4643. https://doi.org/10.1029/2001JD001504

Chen, C.-C., & Gettelman, A. (2016). Simulated 2050 aviation radiative forcing from contrails and aerosols. *Atmospheric Chemistry and Physics*, *16*(11), 7317–7333. https://doi.org/10.5194/acp-16-7317-2016

Conrath, B. J., Hanel, R. A., & Samuelson, R. E. (1989). Thermal structure and heat balance of the outer planets. In S. K. Atreya, J. B. Pollack, & M. S. Matthews (Eds.), *Origin and evolution of planetary and satellite atmospheres*. The University of Arizona Press.

Copernicus Climate Change Service. (2021). CMIP6 predictions underpinning the C3S decadal prediction prototypes [Dataset]. *ECMWF*. https://doi.org/10.24381/CDS.C866074C

Creecy, E. C., Li, L., Jiang, X., Smith, M., Kass, D., Kleinböhl, A., & Martínez, G. (2022). Mars' emitted energy and seasonal energy imbalance. *Proceedings of the National Academy of Sciences of the United States of America*, *119*(21), e2121084119. https://doi.org/10.1073/pnas.2121084119

Creecy, E. C., Li, L., Jiang, X., West, R. A., Fry, P. M., Nixon, C. A., et al. (2021). Titan's global radiant energy budget during the Cassini epoch (2004-2017). *Geophysical Research Letters*, *48*(23), e2021GL095356. https://doi.org/10.1029/2021gl095356

Dessens, O., Köhler, M. O., Rogers, H. L., Jones, R. L., & Pyle, J. A. (2014). Aviation and climate change. *Transport Policy*, *34*, 14–20. https://doi.org/10.1016/j.tranpol.2014.02.014

Dessler, A. E. (2013). Observations of climate feedbacks over 2000–10 and comparisons to climate models. *Journal of Climate*, *26*(1), 333–342. https://doi.org/10.1175/jcli-d-11-00640.1

Dewitte, S., & Clerbaux, N. (2018). Decadal changes of Earth's outgoing longwave radiation. *Remote Sensing*, *10*(10), 1539. https://doi.org/10.3390/rs10101539

Didi, S. R., Diakhaté, M., & Diedhiou, A. (2023). Changes in the West Africa monsoon precipitation extremes during ENSO developing phases. *Atmosphere-Ocean*, *61*(5), 293–305. https://doi.org/10.1080/07055900.2023.2202656

Doelling, D. (2022). CERES Energy Balanced and Filled (EBAF) TOA Monthly means data in netCDF Edition4.2 [Dataset]. *NASA Langley Atmospheric Science Data Center Distributed Active Archive Center*. https://doi.org/10.5067/TERRA-AQUA-NOAA20/CERES/EBAF-TOA_L3B004.2

Ellis, J. S., & Vonder Haar, T. H. (1976). Zonal average Earth radiation budget measurements from satellites for climate studies. In *Colorado State University Atmospheric Science Paper 240*.

Eyring, V., Bony, S., Meehl, G. A., Senior, C. A., Stevens, B., Stouffer, R. J., & Taylor, K. E. (2016). Overview of the Coupled Model Intercomparison Project Phase 6 (CMIP6) experimental design and organization. *Geoscientific Model Development*, *9*(5), 1937–1958. https://doi.org/10.5194/gmd-9-1937-2016

Hanel, R. A., Conrath, B. J., Jennings, D. E., & Samuelson, R. E. (2003). *Exploration of the solar system by infrared remote sensing*. Cambridge University Press.

Hansen, J., Nazarenko, L., Ruedy, R., Sato, M., Willis, J., Del Genio, A., et al. (2005). Earth's energy imbalance: Confirmation and implications. *Science*, *308*(5727), 1431–1435. https://doi.org/10.1126/science.1110252

Hansen, J., Sato, M., Kharecha, P., & von Schuckmann, K. (2011). Earth's energy imbalance and implications. *Atmospheric Chemistry and Physics*, *11*(24), 13421–13449. https://doi.org/10.5194/acp-11-13421-2011

Huang, B., Thorne, P. W., Banzon, V. F., Boyer, T., Chepurin, G., Lawrimore, J. H., et al. (2017). Extended Reconstructed Sea Surface Temperature, Version 5 (ERSSTv5): Upgrades, validations, and intercomparisons. *Journal of Climate*, *30*(20), 8179–8205. https://doi.org/10.1175/JCLI-D-16-0836.1

Huang, H., Huang, Y., & Hu, Y. (2021). Quantifying the energetic feedbacks in ENSO. *Climate Dynamics*, *56*(1–2), 139–153. https://doi.org/10.1007/s00382-020-05469-y

Hunt, G. E., Kandel, R., & Mecherikunnel, A. T. (1986). A history of presatellite investigations of Earth's radiation budget. *Reviews of Geophysics*, *24*(2), 351–356. https://doi.org/10.1029/rg024i002p00351

Jiang, X., Adames, Á. F., Kim, D., Maloney, E. D., Lin, H., Kim, H., et al. (2020). Fifty years of research on the Madden-Julian Oscillation: Recent progress, challenges, and perspectives. *Journal of Geophysical Research: Atmospheres*, *125*(17), e2019JD030911. https://doi.org/10.1029/2019jd030911

Jiang, X., Camp, C. D., Shia, R., Noone, D., Walker, C., & Yung, Y. L. (2004). Quasi-biennial oscillation and quasi-biennial oscillation-annual beat in the tropical total column ozone: A two-dimensional model simulation. *Journal of Geophysical Research*, *109*(D16), D16305. https://doi.org/10.1029/2003jd004377

Jiang, X., Pawson, S., Camp, C. D., Nielsen, J. E., Shia, R. L., Liao, T., et al. (2008a). Interannual variability and trends of extratropical ozone. Part I: Northern Hemisphere. *Journal of the Atmospheric Sciences*, *65*(10), 3013–3029. https://doi.org/10.1175/2008jas2665.1

Jiang, X., Pawson, S., Camp, C. D., Nielsen, J. E., Shia, R. L., Liao, T., et al. (2008b). Interannual variability and trends of extratropical ozone. Part II: Southern Hemisphere. *Journal of the Atmospheric Sciences*, *65*(10), 3030–3041. https://doi.org/10.1175/2008jas2793.1

Kolly, A., & Huang, Y. (2018). The radiative feedback during the ENSO cycle: Observations versus models. *Journal of Geophysical Research: Atmospheres*, *123*(17), 0907–9108. https://doi.org/10.1029/2018jd028401

Larkin, N. K., & Harrison, D. E. (2005). Global seasonal temperature and precipitation anomalies during El Niño autumn and winter. *Geophysical Research Letters*, *32*(16). https://doi.org/10.1029/2005gl022860

Li, C., & Ingersoll, A. P. (2015). Moist convection in hydrogen atmospheres and the frequency of Saturn's giant storms. *Nature Geoscience*, *8*(5), 398–403. https://doi.org/10.1038/ngeo2405

Li, G., Chen, L., & Lu, B. (2023). A physics-based empirical model for the seasonal prediction of the central China July precipitation. *Geophysical Research Letters*, *50*(3), 2022GL101463. https://doi.org/10.1029/2022gl101463

Li, K., & Tung, K. (2023). Solar cycle as a distinct line of evidence constraining Earth's transient climate response. *Nature Communications*, *14*(1), 8430. https://doi.org/10.1038/s41467-023-43583-7

Li, L., Baines, K. H., Smith, M. A., West, R. A., Pérez-Hoyos, S., Trammell, H. J., et al. (2012). Emitted power of Jupiter based on Cassini CIRS and VIMS observations. *Journal of Geophysical Research*, *117*(E11). https://doi.org/10.1029/2012JE004191

Li, L., Guan, L., Li, S., Luu, C., Heng, K., Fry, P. M., et al. (2023). The bolometric Bond albedo of Enceladus. *Icarus*, *394*, 115429. https://doi.org/10.1016/j.icarus.2023.115429

Li, L., Jiang, X., Trammell, H. J., Pan, Y., Hernandez, J., Conrath, B. J., et al. (2015). Saturn's giant storm and global radiant energy. *Geophysical Research Letters*, *42*(7), 2144–2148. https://doi.org/10.1002/2015gl063763

Li, L., Jiang, X., West, R. A., Gierasch, P. J., Perez-Hoyos, S., Sanchez-Lavega, A., et al. (2018). Less absorbed solar energy and more internal heat for Jupiter. *Nature Communications*, *9*(1), 3709. https://doi.org/10.1038/s41467-018-06107-2

Liu, C., Allan, R. P., Mayer, M., Hyder, P., Desbruyères, D., Cheng, L., et al. (2020). Variability in the global energy budget and transports 1985–2017. *Climate Dynamics*, *55*(11–12), 3381–3396. https://doi.org/10.1007/s00382-020-05451-8

Loeb, N. G., Doelling, D. R., Wang, H., Su, W., Nguyen, C., Corbett, J. G., et al. (2018). Clouds and the Earth's Radiant Energy System (CERES) Energy Balanced and Filled (EBAF) Top-of-Atmosphere (TOA) edition 4.0 data product. *Journal of Climate*, *31*(2), 895–918. https://doi.org/10.1175/JCLI-D-17-0208.1

Loeb, N. G., Johnson, G. C., Thorsen, T. J., Lyman, J. M., Rose, F. G., & Kato, S. (2021). Satellite and ocean data reveal marked increase in Earth's heating rate. *Geophysical Research Letters*, *48*(13), e2021GL093047. https://doi.org/10.1029/2021gl093047

Loeb, N. G., Lyman, J. M., Johnson, G. C., Allan, R. P., Doelling, D. R., Wong, T., et al. (2012). Observed changes in top-of-the-atmosphere radiation and upper-ocean heating consistent within uncertainty. *Nature Geoscience*, *5*(2), 110–113. https://doi.org/10.1038/ngeo1375

Loeb, N. G., Mayer, M., Kato, S., Fasullo, J. T., Zuo, H., Senan, R., et al. (2022). Evaluating twenty-year trends in Earth's energy flows from observations and reanalyses. *Journal of Geophysical Research: Atmospheres*, *127*(12), e2022JD036686. https://doi.org/10.1029/2022jd036686

Loeb, N. G., Su, W., Doelling, D., Wong, T., Minnis, P., Thomas, S., & Miller, W. (2018). Earth's top-of-atmosphere radiation budget. *Comprehensive Remote Sensing*, *5*, 67–84. https://doi.org/10.1016/B978-0-12-409548-9.10367-7

Loeb, N. G., Wang, H., Allan, R. P., Andrews, T., Armour, K., Cole, J. N. S., et al. (2020). New generation of climate models track recent unprecedented changes in Earth's radiation budget observed by CERES. *Geophysical Research Letters*, *47*(5), e2019GL086705. https://doi.org/10.1029/2019gl086705

Lorenz, E. N. (1955). Available potential energy and the maintenance of the general circulation. *Tellus*, *7*(2), 157–167. https://doi.org/10.1111/j.2153-3490.1955.tb01148.x

Martin, L. J., & Zurek, R. W. (1993). An analysis of the history of dust activity on Mars. *Journal of Geophysical Research*, *98*(2), 3221–3246. https://doi.org/10.1029/92je02937

Matus, A. V., & L'Ecuyer, T. S. (2017). The role of cloud phase in Earth's radiation budget. *Journal of Geophysical Research: Atmospheres*, *122*(5), 2059–2078. https://doi.org/10.1002/2016JD025951

Mayer, M., Fasullo, J. T., Trenberth, K. E., & Haimberger, L. (2016). ENSO-driven energy budget perturbations in observations and CMIP models. *Climate Dynamics*, *47*(12), 4009–4029. https://doi.org/10.1007/s00382-016-3057-z

Mlynczak, P. E., Smith, G. L., & Doelling, D. R. (2011). The annual cycle of Earth radiation budget from Clouds and the Earth's Radiant Energy System (CERES) data. *Journal of Applied Meteorology and Climatology*, *50*(12), 2490–2503. https://doi.org/10.1175/jamc-d-11-050.1

National Center for Atmospheric Research Staff. (2024). In K. E. Trenberth (Ed.), *Nino SST indices (Nino 1+2, 3, 3.4, 4; ONI and TNI)*.

Peixoto, J. P., & Oort, A. H. (1992). *Physics of climate*. American Institute of Physics.

Philander, S. G. (1990). *El Niño, La Niña, and the Southern Oscillation*. Academic Press.

Pinker, R. T., Grodsky, S. A., Zhang, B., Busalacchi, A., & Chen, W. (2017). ENSO impact on surface radiative fluxes as observed from space. *Journal of Geophysical Research: Oceans*, *122*(10), 7880–7896. https://doi.org/10.1002/2017jc012900

Press, W. H., Teukolsky, S. A., Vetterling, W. T., & Flannery, B. P. (1992). *Numerical Recipes in Fortran 77: The art of scientific computing* (2nd ed., p. 933). Cambridge University Press.

Radley, C., Fueglistaler, S., & Donner, L. (2014). Cloud and radiative balance changes in response to ENSO in observations and models. *Journal of Climate*, *27*(9), 3100–3113. https://doi.org/10.1175/jcli-d-13-00338.1

Read, P. L., Barstow, J., Charnay, B., Chelvaniththilan, S., Irwin, P. G. J., Knight, S., et al. (2016). Global energy budgets and "Trenberth diagrams" for the climates of terrestrial and gas giant planets. *Quarterly Journal of the Royal Meteorological Society*, *142*(695), 703–720. https://doi.org/10.1002/qj.2704

Salby, M. L. (1996). *Fundamentals of atmospheric physics*. Academic Press.

Sánchez-Lavega, A., Río-Gaztelurrutia, T. d., Hueso, R., Gómez-Forrellad, J. M., Sanz-Requena, J. F., Legarreta, J., et al. (2011). Deep winds beneath Saturn's upper clouds from a seasonal long-lived planetary-scale storm. *Nature*, *475*(7354), 71–74. https://doi.org/10.1038/nature10203

Sausen, R., Isaksen, I., Grewe, V., Hauglustaine, D., Lee, D. S., Myhre, G., et al. (2005). Aviation radiative forcing in 2000: An update on IPCC (1999). *Meteorologische Zeitschrift*, *14*(4), 555–561. https://doi.org/10.1127/0941-2948/2005/0049

Shell, K. M., Kiehl, J. T., & Shields, C. A. (2008). Using the radiative kernel technique to calculate climate feedbacks in NCAR's community atmospheric model. *Journal of Climate*, *21*(10), 2269–2282. https://doi.org/10.1175/2007jcli2044.1

Smith, G. L., Mlynczak, P. E., & Potter, G. L. (2012). A technique using principal component analysis to compare seasonal cycles of Earth radiation from CERES and model computations. *Journal of Geophysical Research*, *117*(D9), D09116. https://doi.org/10.1029/2011jd017343

Storto, A., Yang, C., & Masina, S. (2017). Constraining the global ocean heat content through assimilation of CERES-derived TOA energy imbalance estimates. *Geophysical Research Letters*, *44*(20), 10–520. https://doi.org/10.1002/2017gl075396

Stuecker, M. F., Timmermann, A., Jin, F.-F., McGregor, S., & Ren, H.-L. (2013). A combination mode of the annual cycle and the El Niño/Southern Oscillation. *Nature Geoscience*, *6*(7), 540–544. https://doi.org/10.1038/ngeo1826

Su, W., Loeb, N. G., Liang, L., Liu, N., & Liu, C. (2017). The El Niño–Southern Oscillation effect on tropical outgoing longwave radiation: A daytime versus nighttime perspective. *Journal of Geophysical Research: Atmospheres*, *122*(15), 7820–7833. https://doi.org/10.1002/2017jd027002

Trammell, J. H., Jiang, X., Li, L., Kao, A., Zhang, G. J., Chang, E. K. M., & Yung, Y. (2016). Temporal and spatial variability of precipitation from observations and models. *Journal of Climate*, *29*(7), 2043–2055. https://doi.org/10.1175/jcli-d-15-0325.1

Trenberth, K. E., & Fasullo, J. T. (2012). Tracking Earth's energy: From El Niño to global warming. *Surveys in Geophysics*, *33*(3–4), 413–426. https://doi.org/10.1007/s10712-011-9150-2

Trenberth, K. E., Fasullo, J. T., & Balmaseda, M. A. (2014). Earth's energy imbalance. *Journal of Climate*, *27*(9), 3129–3144. https://doi.org/10.1175/jcli-d-13-00294.1

Trenberth, K. E., Fasullo, J. T., O'Dell, C., & Wong, T. (2010). Relationships between tropical sea surface temperature and top-of-atmosphere radiation. *Geophysical Research Letters*, *37*(3), L03702. https://doi.org/10.1029/2009gl042314

Trenberth, K. E., Fasullo, J. T., von Schuckmann, K., & Cheng, L. (2016). Insights into Earth's energy imbalance from multiple sources. *Journal of Climate*, *29*(20), 7495–7505. https://doi.org/10.1175/jcli-d-16-0339.1

Trenberth, K. E., & Stepaniak, D. P. (2001). Indices of El Niño evolution. *Journal of Climate*, *14*(8), 1697–1701. https://doi.org/10.1175/1520-0442(2001)014<1697:lioeno>2.0.co;2

Trenberth, K. E., Zhang, Y., Fasullo, J. T., & Taguchi, S. (2015). Climate variability and relationships between top-of-atmosphere radiation and temperatures on Earth. *Journal of Geophysical Research: Atmospheres*, *120*(9), 3642–3659. https://doi.org/10.1002/2014jd022887

Wang, C., Deser, C., Yu, J.-Y., DiNezio, P., & Clement, A. (2016). El Niño and Southern Oscillation (ENSO): A review. In P. W. Glynn, D. P. Manzello, & I. C. Enochs (Eds.), *Coral Reefs of the Eastern Tropical Pacific: Persistence and Loss in a Dynamic Environment* (pp. 85–106). Springer.

Wang, X., Li, L., Jiang, X., Fry, P. M., West, R. A., Nixon, C. A., et al. (2024). Cassini spacecraft reveals global energy imbalance of Saturn. *Nature Communications*, *15*(1), 5045. https://doi.org/10.1038/s41467-024-48969-9

Wielicki, B. A., Barkstrom, B. R., Harrison, E. F., Lee, R. B., III., Louis Smith, G., & Cooper, J. E. (1996). Clouds and the Earth's Radiant Energy System (CERES): An Earth observing system experiment. *Bulletin of the American Meteorological Society*, *77*(5), 853–868. https://doi.org/10.1175/1520-0477(1996)077<0853:catere>2.0.co;2

Wielicki, B. A., Wong, T., Young, D. F., Barkstrom, B. R., & Lee, R. B., III. (2005). Differences between ERBE and CERES tropical mean fluxes: ENSO, climate change or calibration? In *Paper presented at American Meteorological Society 10th Conference on Atmospheric Radiation*.

Wilcox, L. J., Shine, K. P., & Hoskins, B. J. (2012). Radiative forcing due to aviation water vapour emissions. *Atmospheric Environment*, *63*, 1–13. https://doi.org/10.1016/j.atmosenv.2012.08.072

10.1029/2024JD042611

Zhou, C., Zelinka, M. D., & Klein, S. A. (2016). Impact of decadal cloud variations on the Earth's energy budget. *Nature Geoscience*, *9*(12), 871–874. https://doi.org/10.1038/ngeo2828

Zhou, X., Liu, F., Wang, B., Xiang, B., Xing, C., & Wang, H. (2019). Different responses of East Asian summer rainfall to El Niño decays. *Climate Dynamics*, *53*(3–4), 1497–1515. https://doi.org/10.1007/s00382-019-04684-6

Zhu, P., Wild, M., van Ruymbeke, M., Thuillier, G., Meftah, M., & Karatekin, O. (2016). Interannual variation of global net radiation flux as measured from space. *Journal of Geophysical Research: Atmospheres*, *121*(12), 6877–6891. https://doi.org/10.1002/2015jd024112